ACS APPLIED ENERGY MATERIALS

www.acsaem.org Article

Nanocast Mixed Ni–Co–Mn Oxides with Controlled Surface and Pore Structure for Electrochemical Oxygen Evolution Reaction

Tatiana Priamushko, Rémy Guillet-Nicolas, Mingquan Yu, Matthew Doyle, Claudia Weidenthaler, Harun Tüysüz,* and Freddy Kleitz*

Cite This: *ACS Appl. Energy Mater.* 2020, 3, 5597–5609 Read Online

ACCESS | Metrics & More | Article Recommendations | Supporting Information

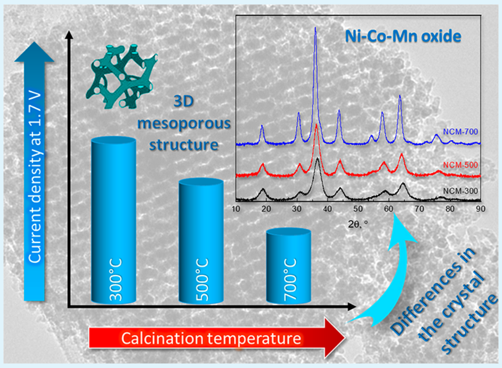

ABSTRACT: Nanocasting or hard-templating is a versatile method to produce ordered mesoporous mixed transition metal oxides (MTMOs) with promising potential for both oxygen evolution reaction (OER) and oxygen reduction reaction (ORR). Herein, a comprehensive investigation was conducted on various $Ni_xCo_yMn_zO_4$ replicated from large pore KIT-6 silica. The materials were calcined at different temperatures to study the influence of the oxide formation and the resulting pore structure ordering, as well as surface properties, on the electrochemical activity and stability of the catalysts. After a comprehensive characterization, electrocatalytic performances of the materials were investigated in detail for OER to find a structure–activity relationship. In OER, a correlation was established between calcination temperature, pore and surface properties, and the overall efficiency and stability. The best sample, $Ni_xCo_yMn_zO_4$ calcined at 300 °C, provided a reasonable current density (25 mA/cm^2 at 1.7 V vs RHE) and an overpotential of 400 mV at 10 mA/cm^2, and demonstrated increased current density (above 200 mA/cm^2 at 1.7 V vs RHE) once loaded into a Ni foam compared to the bare foam. This sample also remained stable over 15 h. Our results indicate that the calcination temperature greatly affects the porosity, crystalline structure, phase composition, and the activity of the catalysts toward OER.

KEYWORDS: *electrocatalysts, OER, mesoporous materials, nanocasting, non-noble metals, mixed metal oxides, spinel*

■ INTRODUCTION

With the increased worldwide concerns surrounding human activities over carbon footprints, the need for readily available chemical power sources, such as fuel cells,[1] metal–air batteries (MABs),[2] and photoelectrochemical (PEC) water splitting devices,[3] has been a focus of major interest. Electrochemical water splitting is a promising way to convert electrical energy into chemical energy (hydrogen), and it is attractive as an alternative green technology for the storage of energy. Water splitting consists of two half reactions: hydrogen evolution reaction (HER) at the cathode and oxygen evolution reaction (OER) at the anode.[4] The HER has a relatively simple reaction mechanism which follows a two-electron pathway.[4] In contrast, OER includes four-electron transfer and an oxygen–oxygen (O–O) bond formation[4,5] which usually result in sluggish reaction kinetics. In alkaline media OER, water (H_2O) and oxygen (O_2) are generated by the oxidation of the hydroxide (OH^-). At equilibrium, 1 atm, and at 25 °C, the half-cell potential (E°_a) for the OER reaction in alkaline electrolyte (pH ∼ 14) is expressed by the following eq 1:[5]

$$4OH^- \leftrightarrow 2H_2O(l) + O_2(g) + 4e^- \qquad E^\circ_a = 0.404\ \text{V} \tag{1}$$

The main problem of the reaction mechanism lies in the fact that single-electron transfers are energetically favorable during the OER compared to multi-electron reactions. This leads to inefficient kinetics and excessive overpotential values due to a buildup of energy at each step.[5] To overcome these issues, it is customary to use electrocatalysts based on noble metals. However, while being highly active, these catalysts are expensive and scarce. Moreover, for some of them, i.e., the highly active ruthenium (Ru), a nonstable oxide layer may grow at the interface during the electrochemical reaction, leading to the corrosion and progressive dissolution of the metal.[6] Therefore, considerable research efforts have recently been devoted to the development of cheaper, earth-abundant, stable, and more efficient catalysts.

In this way, the utilization of first-row transition metals (e.g., Mn, Co, and Ni) is of great interest.[7−9] The advantages of these metals are their low cost and high abundance and their

Received: March 13, 2020
Accepted: May 14, 2020
Published: May 14, 2020

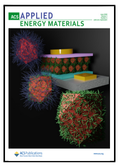

https://dx.doi.org/10.1021/acsaem.0c00544

multiple valent state possibilities in their mixed transition metal oxide (MTMOs) forms.[7] Among these, the spinel structures are the most appealing and spinel-type transition metal oxides have been shown to be effective electrocatalysts for the OER.[5,7,10] Indeed, the spinel structure can accommodate multiple transition metal cations resulting in a variety of valence state possibilities, which is an advantage for OER/ORR. In particular, cobalt-based materials are very promising for energy application with respect to the onset potentials and reaction rates in the OER, even if their performances in ORR are limited.[3,5,6] Unfortunately, due to unreliable supplies and potential toxicity hazards, nowadays cobalt is difficult to import into the European Union (EU) and is classified as an economically unstable and critical raw material.[11] Therefore, combining cobalt with more earth-abundant, cheap, and eco-friendly transition metals is a highly attractive strategy to develop the next generation of materials for storage and conversion of energy.

To do so, various metals appear as interesting options. One of them is manganese (Mn). It is one of the earth's most abundant metals, and some of its oxide forms have been shown to have good catalytic activities toward ORR in alkaline media.[12,13] However, the activity of Mn alone toward OER is still unsatisfactory, preventing its use as a bifunctional catalyst.[7,8] Another cheap non-noble transition metal, nickel (Ni), is a promising OER catalyst, surpassing both cobalt- and platinum-based ones and exhibiting a high stability in alkaline media over prolonged periods of time.[7,14,15] Combination of two or more of these metals in mixed transition metal oxides could thus be of interest for the design of improved electrocatalysts. To date, most research has focused on binary and ternary oxides, such as Co_3O_4, $MnCo_2O_4$, $NiCo_2O_4$, and $NiMn_2O_4$, with the cobaltites attracting particular attention due to their high OER activity.[16−19] The combination of these metals results in noticeable synergistic effects, increasing the bifunctional activity toward the redox reactions of interest. On the other hand, less studies were dedicated to the investigation of quaternary MTMOs despite their potential regarding the catalytic activity for OER and/or ORR.[7] Yu and Manthiram[20] found that $(Ni,Mn,Co)_3O_4$ nanoparticles supported on nitrogen-doped multiwall carbon nanotubes exhibited excellent bifunctional catalytic activity for both ORR and OER. Recently, Sivakumar et al.[21] synthesized $(Ni,Mn,Co)_3O_4$ spinel oxide nanoparticles with different compositions and investigated their bifunctional catalytic activity toward ORR and OER, the $NiCoMnO_4$ electrocatalysts showing promising results. Similar approaches and results were reported by Pendashteh et al.[22] In particular, the $(Ni,Mn,Co)_3O_4$ nanoparticles anchored on graphene resulted in an efficient non-precious-metal-based bifunctional catalyst for ORR and OER, with superior durability compared to a commercial platinum/carbon (Pt/C) catalyst.[22] Similarly, the spinel oxide nanoparticles demonstrated good ORR and OER performances with catalytic activity comparable to the one of IrO_2 in the latter reaction.[21,22] These works demonstrated that the $(Ni,Mn,Co)_3O_4$ system might be a promising catalyst toward OER.

Regarding the physicochemical parameters of these electrocatalysts, different reports emphasized the importance of the porosity and morphology in the activity and stability of the catalyst.[6,23] Mesoporous cobalt oxide Co_3O_4 had superior activities in comparison to its nanoparticle-based counterparts, especially considering its activity and stability toward water oxidation.[24,25] Moreover, the mesoporous network was also shown to better retain the Co_3O_4 nanostructure, avoiding catalytic degenerative processes, i.e., aggregation and sintering.[26] Nanocasting, or hard-templating, is one of the most straightforward approaches to synthesize mesoporous metal-based materials with tunable pore size, pore volume, specific surface area (SSA), and morphology.[25,27−29] This technique allows for the synthesis of replicas with ordered and/or three-dimensional (3D) pore networks, crystalline structures, and good thermal stability.[30,31] For instance, Ren et al.[32] reported the first synthesis of ordered mesoporous $(Ni,Mn,Co)_3O_4$, with spinel crystalline structure via the hard-templating route. This material was investigated for energy storage and catalytic decomposition of N_2O. This mesoporous $(Ni,Mn,Co)_3O_4$ showed greater catalytic activities as compared to the nonporous β-MnO_2 and γ-MnO_2. This result was rationalized considering the critical role played by the surface area and accessibility of the active sites of the mesoporous $(Ni,Mn,Co)_3O_4$. Moreover, due to the presence of Ni and Co, the activities in both OER and ORR were higher than the ones observed for other bimetallic compositions, i.e., $LiMn_2O_4$ and $CuMn_2O_4$, with similar BET surface areas, highlighting the importance of the synergy between the transition metals.[33] This is in agreement with the work of Sivakumar et al.[21] where $(Ni,Mn,Co)_3O_4$ spinel nanoparticles also outperformed $MnCo_2O_4$, $NiCo_2O_4$, and NiO oxides. However, while chemical composition, stoichiometry, and surface area effects are typically studied, there are much less data available so far on the effects of the oxide formation and pore structure of mesoporous quaternary MTMOs on their resulting electrocatalytic activity and stability. To get more insights into such effects, we propose a systematic study of mesoporous trimetallic MTMOs obtained via nanocasting. In this work, the highly ordered 3D mesoporous silica KIT-6 was chosen as the template since it is well-known to yield mesoporous transition metal oxide replicas of excellent quality.[25,34−36] The resulting 3D ordered mesoporous oxides were characterized by N_2 physisorption at −196 °C (77 K), powder X-ray diffraction (PXRD), electron microscopy, and X-ray photoelectron spectroscopy (XPS). Electrocatalytic performances and stability of the mesoporous MTMO catalysts were studied in detail, and the correlation between calcination temperature, porosity, and surface properties onto overall efficiency was established. As such, our results provide perspectives for the successful preparation of efficient electrocatalysts and highlight the potential of mesoporous MTMOs as catalysts for OER.

■ MATERIALS AND METHODS

Synthesis of Ordered Mesoporous Silica. The 3D cubic ordered mesoporous KIT-6 was synthesized according to Kleitz et al.[37] The copolymer poly(ethylene oxide)-*block*-poly(propylene oxide)-*block* poly(ethylene oxide) (Pluronic P123, $EO_{20}PO_{70}EO_{20}$, Sigma-Aldrich, Germany) was used as the structure-directing agent. In a typical synthesis, 5.13 g of Pluronic P123 was first dissolved in a solution of concentrated HCl (9.92 g, 37%, Sigma-Aldrich, Germany) and distilled water (185.33 g). This mixture was stirred at 35 °C until complete dissolution of the polymer. Then, *n*-butanol (5.13 g, 99%, Thermo Fisher Scientific, Germany) was added at once under the stirring as a co-structure-directing agent, and the mixture was stirred overnight at 35 °C. An 11.03 g amount of TEOS (tetraethyl orthosilicate, Sigma−Aldrich, Germany) was added to the solution in one shot, followed by stirring at 35 °C for 24 h. Afterward, the mixture was heated at 100 °C for 48 h in a convection oven (Binder, Germany). The resulting white solid product was filtered hot without washing and dried for 2 h at 100 °C and then overnight at 140 °C. Subsequently, the powder was extracted in a solution of 200 mL of ethanol (96%, Brenntag, Austria) in which 2 drops of concentrated HCl (37%) were added. Finally, the silica material was calcined in air at 550 °C (heating ramp $\approx$ 1.5 °C/min) for 3 h.

Synthesis of Ordered Mixed Metal Oxides. Three-dimensional ordered mesoporous oxides were synthesized using the incipient wetness nanocasting method.[28] Metal nitrates ($Co(NO_3)_2 \cdot 6H_2O$, $Mn(NO_3)_2 \cdot 4H_2O$, and $Ni(NO_3)_2 \cdot 6H_2O$) were used as metal precursors as purchased (Thermo Fisher Scientific, Germany). The amount of the saturated solution of the nitrate salts was calculated as 80% of the total pore volume of the silica template. For the synthesis of trimetallic $Ni_xCo_yMn_zO_4$ samples, the nitrates were taken in the stoichiometric proportion of 1:1:1. The precursor solution was mixed with 1 g of degassed (150 °C in a vacuum oven overnight) KIT-6 silica via multiple impregnation steps. The resulting mixture was dried overnight at 70 °C and then calcined at 500 °C (for NiO, Mn_xO_y, and Co_3O_4) and at 300, 500, and 700 °C for $Ni_xCo_yMn_zO_4$ in order to distinguish the effect of the calcination temperature. These samples are named $Ni_xCo_yMn_zO_4$-300, -500, and -700, respectively. The heating ramp was 1 °C/min in every case. The silica template was then selectively removed by treating the powders 3 times with concentrated NaOH (2 M, 24 h at room temperature). Finally, the samples were washed 3 times with distilled water and 3 times with ethanol and dried at 70 °C overnight under air.

Materials Characterization. The porosity and textural properties of the samples were analyzed using N_2 physisorption isotherms measured at −196 °C on a Anton Paar Quantatech Inc. iQ2 instrument (Boynton Beach, FL, USA). The samples were outgassed under vacuum at 150 °C for 12 h prior to measurement. The specific surface area (SSA) was calculated using the Brunauer−Emmett−Teller (BET) equation applied to data points measured in the relative pressure range $0.05 \leq P/P_0 \leq 0.3$. Relevant pore size distributions were calculated from both desorption and adsorption branches of the isotherms by applying the nonlocal density functional theory (NLDFT) kernels of equilibrium and metastable adsorption, respectively, considering an amorphous SiO_2 surface and a cylindrical pore model. Total pore volume (for the pores smaller than 40 nm) was determined using the Gurvich rule.[38] The calculations were carried out using the ASiQwin 5.2 software provided by Anton Paar Quantatech Inc.. The X-ray diffractograms were recorded on a PANalytical EMPYREAN powder diffractometer equipped with the PIXcel^{3D} detector (Malvern PANalytical, United Kingdom) in reflection geometry (Bragg−Brentano HD) using Cu $K\alpha_{1/2}$ radiation, operated at a voltage of 45 kV and a tube current of 40 mA, with a fixed divergence slit of 0.05 mm. Low-angle diffraction data were also collected in transmission geometry (Focusing Mirror). Measurements were performed in continuous mode with a step size 2θ of 0.013° and a data time per step of 300 s (reflection) or 50 s (transmission). In situ PXRD measurements were performed during the heating of KIT-6 template impregnated with the metal precursor solution in order to follow the formation of the spinel structures. PXRD patterns were collected every 25 °C; the material was heated to 900 °C under air with a heating rate of 1 °C/min using a Bruker D8-Advance powder X-ray diffractometer with a reaction chamber XRK900, Anton Paar. A linear position sensitive detector LynxEye was used with the following parameters: opening of 2° 2θ and resolution ~ 0.01° of 2θ. A MACOR sample holder was used. High-resolution TEM (HR-TEM) and scanning electron microscopy (SEM) images were taken on HF-2000 and Hitachi S-5500 microscopes, respectively. Energy dispersive X-ray spectroscopy (EDX) measurements were conducted using two different instruments. A Hitachi S-3500N was used for high-quality elemental mapping of $Ni_xCo_yMn_zO_4$-300, whereas the elemental mapping of all other samples was performed using an EDX detector (Oxford Instruments) as additional equipment for a Zeiss Supra 55 VP scanning electron microscope (Faculty Center for Nano Structure Research, University of Vienna, Vienna, Austria). The Hitachi S-3500N microscope is equipped with a Si(Li) Pentafet Plus-Detector from Texas Instruments. X-ray photoelectron spectroscopy (XPS) measurements were carried out with a SPECS GmbH spectrometer with a hemispherical analyzer (PHOIBOS 150 1D-DLD). The monochromatized Al $K\alpha$ X-ray source (E = 1486.6 eV) was operated at 100 W. An analyzer pass energy of 20 eV was applied for the narrow scans. The medium area mode was used as lens mode. The base pressure during the experiment in the analysis chamber was 5×10^{-10} mbar. The binding energy scale was corrected for surface charging by use of the C 1s peak of contaminant carbon as reference at 284.5 eV.

Electrochemical Measurements. Electrochemical water oxidation measurements were carried out in a typical three-electrode configuration using a rotating disc electrode (RDE, model AFMSRCE, PINE Research Instrumentation), a hydrogen reference electrode (RE, HydroFlex, Gaskatel), and Pt wire as a counter electrode. A 1 M KOH solution purged with argon was used as the electrolyte. The temperature of the cell was kept at 25 °C by using a water circulation system. Modified glassy carbon (GC) electrodes (PINE, 5 mm diameter, 0.19625 cm^2 area) were used as working electrodes. Before use, the surfaces of the GC electrodes were polished with Al_2O_3 suspension (5 and 0.25 μm, Allied High Tech Products, Inc.), followed by sonication in deonized pure water (18.2 MΩ·cm) for 5 min. Then, 4.8 mg of the catalyst was dispersed in a solution containing 0.75 mL of 18.2 MΩ·cm H_2O, 0.25 mL of 2-propanol, and 50 μL of Nafion (around 5% in a mixture of water and lower aliphatic alcohols). The suspension was sonicated for 30 min to form a homogeneous ink. A 5.25 μL aliquot of the catalyst ink was dropped onto the GC electrode and dried under light irradiation. The catalyst loading was calculated to be 0.12 mg/cm^2 in all cases. The $Ni_xCo_yMn_zO_4$-300/Ni foam electrode was fabricated by drop-casting the catalyst ink on the surface of pretreated Ni foam and was dried at room temperature. The loading was around 0.5 mg/cm^2.

In all measurements, the *iR* drop (voltage drop) was automatically compensated for 85% using the potentiostat software (EC-Lab V10.44). All linear scanning voltammetry (LSV) curves were collected by sweeping the potential from 0.7 to 1.7 V vs RHE with a rate of 10 mV/s. Cyclic voltammetry (CV) measurements were carried out in the potential range between 0.7 and 1.6 V vs RHE with a scan rate of 50 mV/s. The activation of catalysts was achieved by conducting continuous scanning of 200 CVs on each sample, and LSV curves were collected before and after the CVs. The reproducibility of the electrochemical data was checked on multiple electrodes. The GC electrodes were kept rotating at a speed of 2000 rpm when LSV and CV curves were being measured. The electrochemical impedance spectroscopy (EIS) was carried out in the same configuration with application of an anodic polarization potential of 1.6 V vs RHE on the working electrode. The spectra were collected from 10^5 to 0.1 Hz with an amplitude of 5 mV. The electrocatalytic active surface area (ECSA) was determined by measuring the non-Faradaic capacitance current associated with double-layer charging from the scan-rate dependence of CVs. CV scans with different scan rates, ranging from 20 to 180 mV s^{-1}, were carried out in a narrow potential window from 1 to 1.1 V vs RHE. By plotting the capacitive current ($\Delta j = j_{\mathrm{anode}} - j_{\mathrm{cathode}}$) against the scan rate and fitting it with a linear fit, the double-layer capacitance (C_{dl}) can be estimated as half of the value of the slope. The ECSA of each sample was calculated from its C_{dl} according to this equation: ECSA = C_{dl}/C_s, where C_s is the specific capacitance. In this work, 0.04 mF/cm^2 was chosen as the reference value of the catalysts for OER in 1 M KOH solution.[39] Stability tests were carried out on a Ni-foam electrode. The potential was recorded at a constant current density of 10 mA/cm^2 over a period of 15 h.

RESULTS

Structure, Porosity, and Composition Analysis. The synthesis of high-quality MTMOs following the nanocasting method requires the production of initial templates with controlled and adequate properties.[40] In this work, we used a 3D-ordered mesoporous KIT-6 hydrothermally treated at 100 °C as the mold, synthesized via a method known to yield reproducible and high-grade samples.[37] The mesoporous ordering and overall quality of the starting material was verified by low-angle XRD measurements and N_2 at −196 °C physisorption analysis (Supporting Information Figure S1). The KIT-6 exhibits the expected cubic *Ia*3*d* pore symmetry and a typical type IVa isotherm with a sharp H1 hysteresis loop,[38] being characteristic of mesoporous materials with a well-defined mesostructure and pores larger than 4 nm. The NLDFT pore size distribution (PSD) indicates a narrow distribution, centered at 8.8 nm (Table 1, Figure S1c). The specific surface area of the KIT-6 powder is 845 m^2/g, and it has a total pore volume of 1.3 cm^3/g (Table 1).[38] The nanocasting method includes two main synthesis steps, these being the infiltration of the template pore network with the precursor of interest, followed then by solidification/oxidation and phase transition, in some cases. The impregnation step was performed using the incipient wetness technique, which allows the successful confinement of high metal precursor loadings. After calcination and silica removal, the physicochemical properties of the resulting replicas were investigated. Figure 1a shows N_2 at −196 °C physisorption isotherms of $Ni_xCo_yMn_zO_4$-300, -500, and -700. The materials all exhibit type IVa isotherms, as expected for mesoporous materials, with complex hysteresis loops that resemble H3 type, although these cannot be fully assigned to this type and may rather be hybrid ones. Indeed, in our case the lower limit of the desorption branch is not closing at the cavitation-induced relative pressure[38] and no significant pore blocking effect was found by comparing the very similar NLDFT pore size distribution curves obtained from the desorption and adsorption branches (Figure 1b and Figure S2). The slightly larger mode pore sizes obtained systematically from the desorption branches might be correlated with the interconnected pore architecture of these replicas, even if one has to remain cautious in the data interpretation since these materials are complex and far from the calibrated models used for calculations. Nevertheless, the pore network of all of the replicas does not exhibit any constricted pores with openings below 4−5 nm that could strongly limit diffusion and mass transport phenomena.[38,41] NLDFT pore size analysis revealed a relatively narrow PSD for $Ni_xCo_yMn_zO_4$-300 and slightly broader ones for the two other samples. Trimetallic samples also have a larger mode pore size as compared to the single oxides, i.e., Co_3O_4 and NiO (Table 1 and Figure S3b), which are known to be easily replicated via nanocasting.[25,39,42] These latter two materials have very similar textural properties (Figure S3) which are in agreement with previously published reports.[25,39,42] However, the Mn_xO_y replica showed different parameters. In addition to a larger SSA and total pore volume, the NLDFT PSD indicated a bigger amount of the larger pores as compared to the other oxides. This behavior can be correlated with the lower quality of the replica, as indicated by the low-angle XRD data (Figure 2a).

Table 1. Specific Surface Area, Pore Size, and Pore Volume of the Materials

sample	BET specific surface area, m^2/g	total pore vol, cm^3/g	NLDFT (desorption) pore size, nm	NLDFT (adsorption) pore size, nm
KIT-6-100	845	1.3	8.8	8.5
Co_3O_4 (-500)	111	0.2	4.9	4.9
NiO (-500)	99	0.2	4.9	4.9
Mn_xO_y (−500)	160	0.5	8.2	29
$Ni_xCo_yMn_zO_4$-300	194	0.6	8.1	7.3
$Ni_xCo_yMn_zO_4$-500	170	0.5	9.1	8.5
$Ni_xCo_yMn_zO_4$-700	143	0.4	9.4	9.4

The calcination temperature of the confined metal salt precursors is a critical parameter during the nanocasting; i.e., despite the potential negative effects of high temperatures that may impair mesopore ordering and phase composition of the replica, they are often required to obtain the desired oxide structure, with given phase and stoichiometry. Therefore, $Ni_xCo_yMn_zO_4$ trimetallic oxides were calcined at different temperatures to rationalize the effect of the calcination temperature on the material and its subsequent electrocatalytic behavior. As it can be seen from Table 1, increasing the calcination temperature during the nanocasting process leads to replicas with lower SSA and total pore volume and larger mode pore size. This effect may be attributed to the formation and growth of bigger crystal domains as well as a more pronounced shrinkage of the oxide mesostructure. To gain more insights into the crystalline characteristics, phase composition, and mesoporous structure of the trimetallic

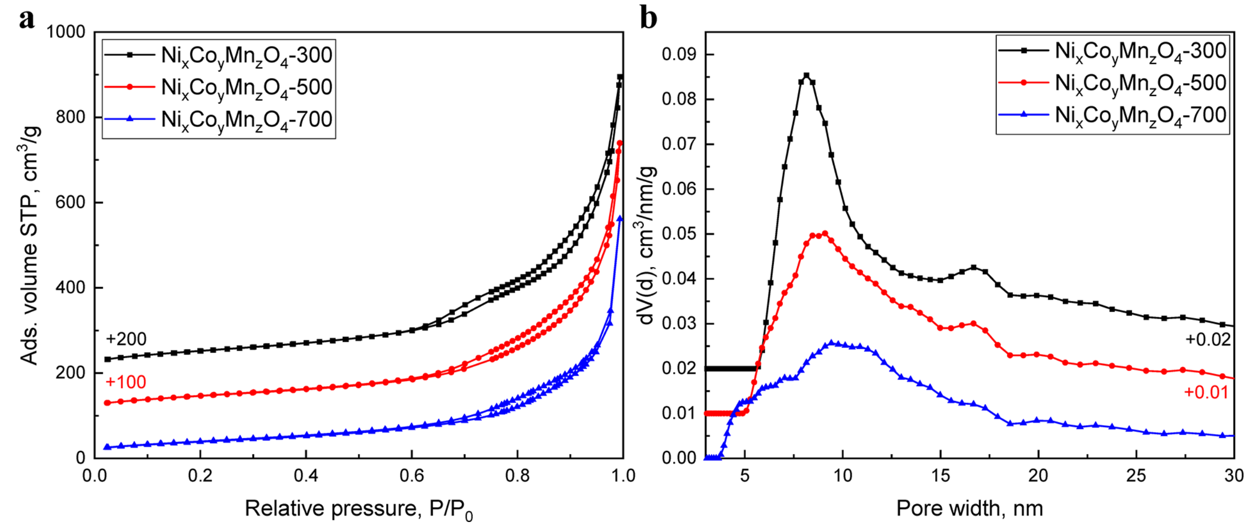

Figure 1. N_2 physisorption isotherms measured at −196 °C (a) and NLDFT pore size distributions (b) of $Ni_xCo_yMn_zO_4$-300, -500, and -700.

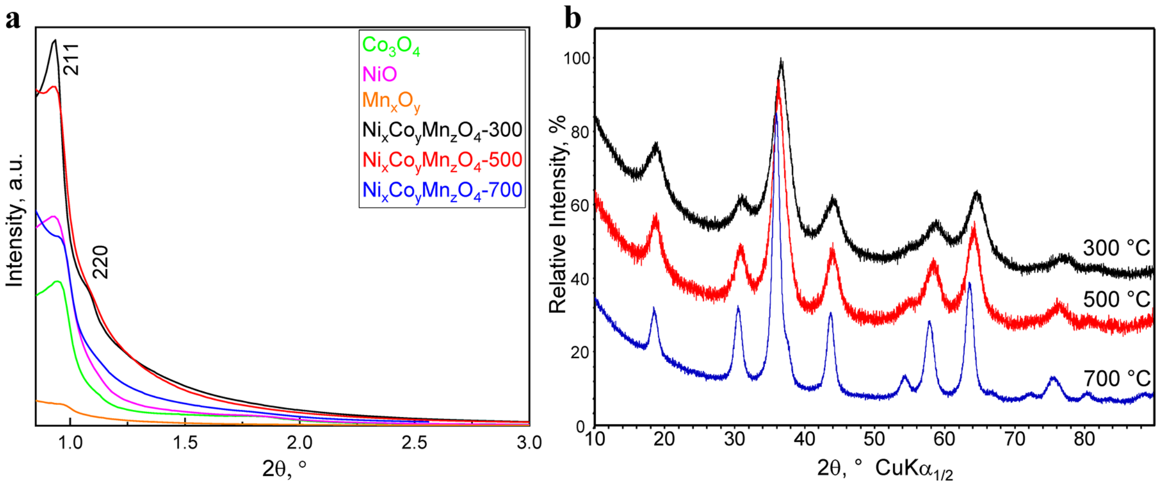

Figure 2. Wide-angle (a) and low-angle (b) XRD patterns of $Ni_xCo_yMn_zO_4$-300, -500, and -700.

replicas, powder X-ray diffraction experiments were conducted and are presented in Figure 2.

Figure 2a shows the data obtained from low-angle XRD measurements. A general decrease in the mesoscopic order is observed with increasing calcination temperatures. Indeed, for $Ni_xCo_yMn_zO_4$-300 one can note the clear presence of the 211 and 220 reflections which are characteristic of the 3D KIT-6 body-centered cubic *Ia*3*d* space group. However, for $Ni_xCo_yMn_zO_4$-500 and -700, the 220 peak, while being present, is not well resolved, indicating a less defined ordered structure. The intensity of the 211 reflection is also lowered for both materials as compared to $Ni_xCo_yMn_zO_4$-300. Single oxides showed reduced intensities of the 211 and 220 reflections. TEM investigations, presented in Figure 3a−c and Figure S4, further confirmed the XRD analyses. For $Ni_xCo_yMn_zO_4$-300 and -500, the pores are well-ordered over relatively large domains, while the sample aged at 700 °C showed a less ordered structure even though it remained highly porous. Figure 2b presents the wide-angle XRD patterns of $Ni_xCo_yMn_zO_4$-300, -500, and -700. In principle, the diffraction patterns match with the spinel structure. No impurities such as NiO or Mn_xO_y are visible (Figure S5a). With increasing calcination temperature, the reflection positions shift to lower angles, indicating an increase of the unit cell parameters. Depending on the calcination temperature, crystal domains of different sizes are formed (Figure 2b). Increasing the temperature leads to narrower reflections, being in line with larger crystal domains. To gain additional insight into these phase evolutions occurring during thermal treatment of the material, we performed high-temperature in situ powder XRD measurements (Figure S5b). In addition, under these conditions, sample preparation effects and possible shift of the reflections caused by sample displacement are limited. From these data, it is seen that at the early stages (300−500 °C) of the formation of the $Ni_xCo_yMn_zO_4$ spinel-type structure, the PXRD patterns demonstrate broad reflections. We assume that the samples calcined at lower temperatures consist of a mixture of Co-rich spinel phases, such as Co_3O_4 and $NiCo_2O_4$, and $NiMn_2O_4$ spinel, which also exhibit cubic *Fd*3*m* space group.[18,24,43,44] Increasing the temperature leads to the increased intensities of the reflections and their positions shifted to lower angles, which correlates well with the reference patterns of the $NiCoMnO_4$ spinel phase.[45,46] It was observed that the actual $NiCoMnO_4$ spinel phase can be formed only at >700 °C, which is in agreement with the previous results.[32]

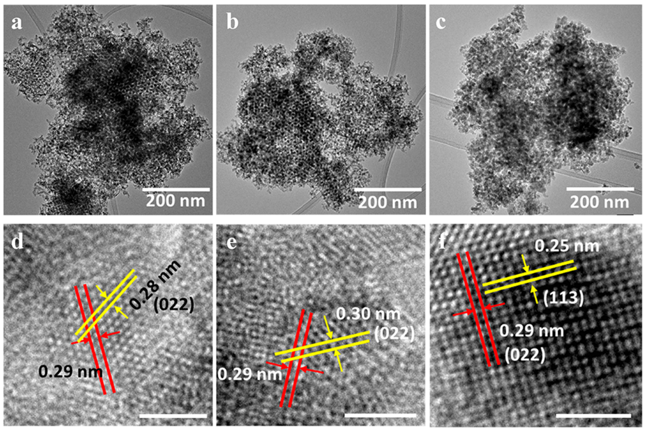

Figure 3. TEM and HR-TEM images of $Ni_xCo_yMn_zO_4$-300 (a, d), $Ni_xCo_yMn_zO_4$-500 (b, e), and $Ni_xCo_yMn_zO_4$-700 (c, f). HR-TEM scale bar: 2 nm.

Subsequently, Rietveld refinements of the powder XRD patterns of the individual materials calcined at the different temperatures were performed to determine phase composition more accurately. The results of the Rietveld refinement performed for $Ni_xCo_yMn_zO_4$-300, -500, and -700 are presented in Figure S6a−-c and Table S1. The Rietveld refinements reveal for $Ni_xCo_yMn_zO_4$-300 that the sample is not composed of a single phase. The Rietveld refinement plot shows a significant mismatch between experimental and theoretical data (Figure S6a). The addition of a second spinel phase (i.e., Co_3O_4) improves the refinement. However, there are still discrepancies which may be caused by structural disorder and/or defects.

The largest lattice parameter (8.2843(2) Å) was found for $Ni_xCo_yMn_zO_4$-700, and the data demonstrate the expansion of the lattice cell with increasing calcination temperature. The lattice parameter is in good correlation with the published work of Ren et al.[32] These authors assumed that annealing at higher temperatures leads to the expansion of the unit cell, which is caused by more intensive incorporation of the larger cations, such as Ni^{2+} and Mn^{3+}, into the spinel structure. However, in our case, although the lattice parameter increase is observed and its value is in line with the published refinement,

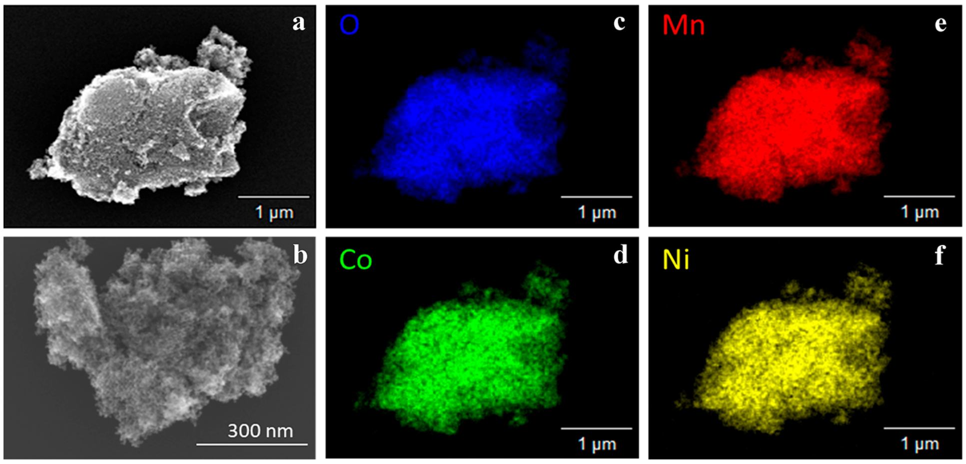

Figure 4. SEM image (a), STEM image (b), and elemental mapping (c−f) of $Ni_xCo_yMn_zO_4$-300.

not all positions are occupied by the same metal cations as it is described by Ren and co-authors.[32] This might indicate the defective structure of the material. Even though this sample demonstrates the closest to $NiCoMnO_4$ structure, the determined lattice parameter does not reach the value of the pure $NiCoMnO_4$ spinel (8.3−8.4 Å).[45,46]

The difference in the lattice parameters was further confirmed using HR-TEM where selected areas were used to calculate the *d*-spacing of the crystals and identify the facets (Figure 3d−f). However, considering that $Ni_xCo_yMn_zO_4$-300 and -500 consist of the mixtures of several phases and have smaller *d*-spacing, it remains difficult to clearly identify the facets from the HR-TEM images. For these samples, some of the facets could be identified and ascribed to $NiCo_2O_4$ (Figure 3d) and $NiMn_2O_4$ (Figure 3e). Differently, in the case of $Ni_xCo_yMn_zO_4$-700, facets can be unambiguously identified and calculated values of *d*-spacing are in line with the reference crystallographic data (Figure 3f).

The elemental distribution in the trimetallic oxides was probed using both bulk and spot EDX-STEM elemental mapping. Tables S2−S4 present bulk EDX data for the samples $Ni_xCo_yMn_zO_4$-300, -500, and -700, respectively. The ratio between the metals is close to 1:1:1 throughout the whole probed area for each sample, which means that the mixture of the different spinel phases in the samples obtained at 300 and 500 °C is very homogeneous. Negligible amounts (less than 1 at. %) of Na and Si are still present in $Ni_xCo_yMn_zO_4$-300 and -500 due to the removal of the silica template with a concentrated NaOH solution during the last step of the nanocasting procedure. Higher amounts of Si (≈2 at. %) remain in $Ni_xCo_yMn_zO_4$-700 due to the higher calcination temperature and its possible effect onto the template−precursor interactions; i.e., stronger bonds might occur and less soluble metal silicates might be formed locally making the silica removal process more difficult.[31,47] Similar results were observed with spot EDX analysis, as shown in Figure S7a−c and corresponding Tables S5−S7. Moreover, as shown in Figure 4 for $Ni_xCo_yMn_zO_4$-300, the metals are indeed evenly distributed through the particles and there is no variation in the elemental ratio, pointing to the chemical homogeneity of all of the samples regardless of the calcination temperature. Figures S8 and S9 show SEM and STEM images of $Ni_xCo_yMn_zO_4$-300 and -500 and overall elemental mapping of $Ni_xCo_yMn_zO_4$-300, -500, and -700. For all samples under investigation, the distribution of the metals does not appear to change, confirming the results of spot and bulk EDX. Morphology studies, including SEM characterization, of the reference materials, i.e., single metal oxides and the parent KIT-6 silica template, can be found in the literature.[48]

Surface information regarding the different chemical oxidation states of the metals was extracted from high-resolution XPS as shown in Figure 5. Ni 2p spectra are almost identical for the three samples. They reveal two characteristic peaks centered around 855.0−855.2 and 872.6−873.1 eV, assigned to the Ni $2p_{3/2}$ and Ni $2p_{1/2}$ spin−orbit levels, respectively, which are attributed to Ni^{2+} species.[22,49] The spectra are similar to the spectrum of $Ni(OH)_2$, which might indicate the existence of surface OH groups originating from the conditions used for the removal of the template, as already mentioned above. Spectra of the Co 2p core level present two clear spin−orbit doublets assigned to Co $2p_{3/2}$ and Co $2p_{1/2}$ (Figure 5b), correlating with previous data in the literature.[16,50−52] The shakeup peaks of Co 2p can be used for identification of the oxidation state of cobalt. Increasing the calcination temperature changes the Co^{2+}/Co^{3+} surface ratio of the $Ni_xCo_yMn_zO_4$ samples. For the material calcined at 300 °C, both Co^{2+} and Co^{3+} species are present on the surface with a slightly increased amount of Co^{2+} as compared to the reference spinel Co_3O_4.[51,52] These results correlate with the assumption that calcination at 300 °C might have led to the formation of a mixture of Co-rich spinel phases, e.g., Co_3O_4, $NiCo_2O_4$, and so on, where Co has an oxidation state 3+. $Ni_xCo_yMn_zO_4$ calcined at 500 °C show less surface Co^{3+} species compared to $Ni_xCo_yMn_zO_4$-300, making Co^{2+} species predominant. Increasing the temperature up to 700 °C might lead to the self-reduction of Co^{3+} to Co^{2+} species on the surface of the oxide.[53,54] O 1s spectra (Figure 5c) consist of two peaks centered around 529.6−529.8 and 531.2−531.4 eV for each sample that are attributed to M−O−M (M = Ni, Co, or Mn) and OH groups, respectively.[55] The oxidation state of Mn can be distinguished using the Mn 3s peak. As can be seen in the Figure 5d, this peak has two components arising from the multiple splitting induced by the coupling of non-ionized 3s electrons with 3d valence-band ones.[55] The distance between these two peaks is an indication of the oxidation state of Mn. Here, all samples show a ΔE value close to 4.8 eV, which is attributed to Mn^{4+}.[22,38]

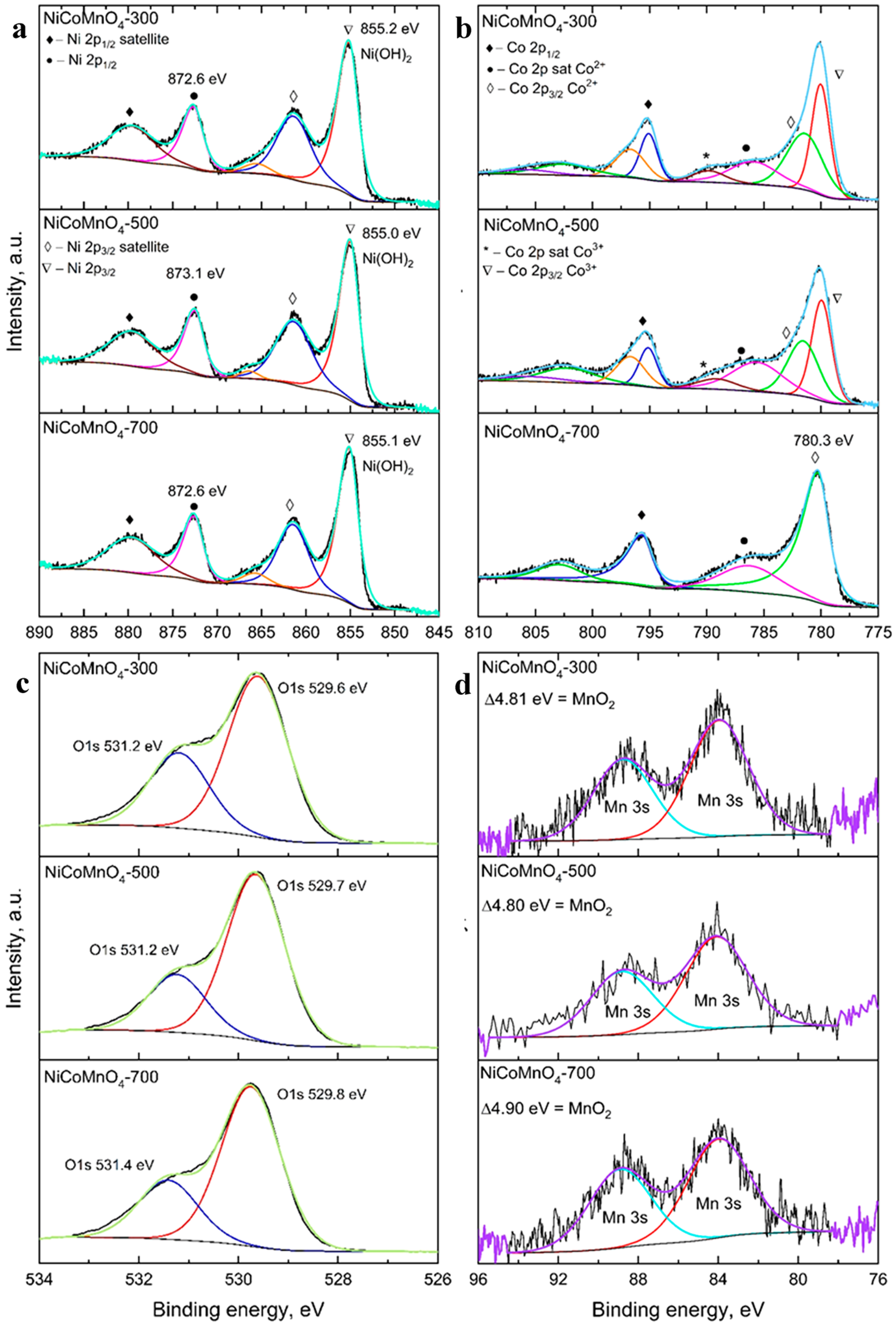

Figure 5. XPS analysis of $Ni_xCo_yMn_zO_4$: high-resolution spectra of Ni 2p (a), Co 2p (b), O 1s (c), and Mn 3d (d).

Electrocatalytic Performance. OER performances of the materials were investigated following a protocol previously published.[56] To assess electrocatalytic activity, the catalyst was loaded on a glassy carbon electrode (GCE), as described in Materials and Methods, and subjected to cyclic voltammetry measurements in Ar-saturated 1 M KOH solution followed by LSV measurements after intervals of 50 CV cycles. For comparison purposes, a loading of 0.12 mg/cm^2 was kept for all oxide catalysts. Figure S10a−c shows CV curves for $Ni_xCo_yMn_zO_4$-300, -500, and -700, respectively. $Ni_xCo_yMn_zO_4$-300 shows two oxidation peaks (Figure S10a). The first one is sharp and narrow and might be attributed to the oxidation of metal species with +2 oxidation state located in the tetrahedral sites. The second peak, being relatively weak and broader, could represent the oxidation of Mn^{3+} or Co^{3+} located in the octahedral sites of the spinel structure.[21,22] The component of each single oxidation peak coming from the different single oxide becomes clearer when compared with the CV profiles of single oxides (Figure S10d−f). $Ni_xCo_yMn_zO_4$-500 and -700 only exhibit one broad peak, which can be mainly ascribed to the oxidation of Ni^{2+} rather than the oxidation of Co^{3+}. This assumption is in line with the smaller amount of Co^{3+} species on the surface of $Ni_xCo_yMn_zO_4$-500, and -700 detected via XPS. Clearly, the calcination temperature has a direct effect on the characteristics of the voltammogram. Noticeably, the center of the oxidation peaks is shifted to

https://dx.doi.org/10.1021/acsaem.0c00544
ACS Appl. Energy Mater. 2020, 3, 5597−5609

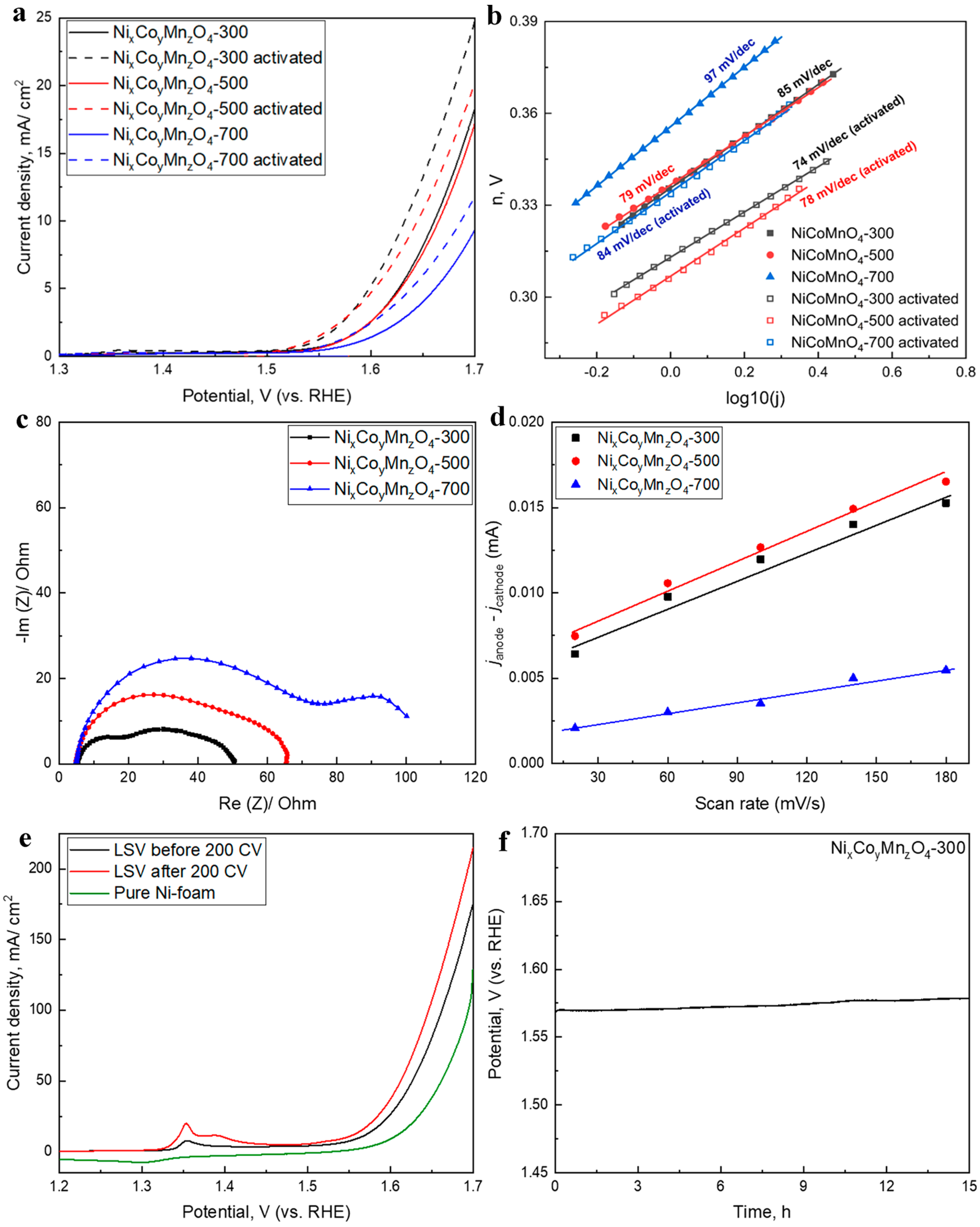

Figure 6. Initial and activated (after 200 CV cycles) LSV curves (a), initial and activated Tafel slopes (b), the Nyquist plots (c), and capacitive current difference at 1.05 V (vs RHE) against scan rates (d) for $Ni_xCo_yMn_zO_4$ samples; initial and activated LSV curves (e), and chronopotentiometric test (f) of $Ni_xCo_yMn_zO_4$-300 loaded on Ni foam at a current density of 10 mA/cm^2.

higher potentials for the samples calcined at higher temperatures, which gives a hint for alteration of the surface structure of the materials. In addition, several works[57−59] have pointed out that the structurally strained and unstable Co^{4+} species on the surface can act as intermediate species for OER. Therefore, among the $Ni_xCo_yMn_zO_4$ samples, $Ni_xCo_yMn_zO_4$-300 appears as the most promising catalyst.

As we mentioned before, LSV measurements were performed after every 50 cycles to follow the activation process. As expected, among all $Ni_xCo_yMn_zO_4$ samples, $Ni_xCo_yMn_zO_4$-300 demonstrated the highest activity before and after 200 cycles (Figure 6a and Figure S11a−c). It can be seen from the associated CV results that the activated materials achieved increased current densities. This increased activity seemed to be a direct consequence of (1) conversion of metal oxides to their oxyhydroxide counterparts that possess much higher OER activity or (2) the incorporation of Fe impurities from the KOH electrolyte into the Ni-containing catalyst surface that results in the formation of an active metal coordination environment.[60,61] Lower overpotentials (Table S8) were also found after activation, being in line with previously published results.[20,22] However, the activity of the

$Ni_xCo_yMn_zO_4$-500 catalyst after 200 CVs, considering the current density at 1.7 V, is still lower than that of $Ni_xCo_yMn_zO_4$-300 (Figure 6a). Figure 6b shows the Tafel plots, which were extracted from the LSV curves before and after activation, for the $Ni_xCo_yMn_zO_4$ samples. The Tafel slopes of the single oxides are presented for comparison in Figure S12a. The final values are listed in Table S8. The values of the initial Tafel slopes are in the range of 79−97 mV/dec for the $Ni_xCo_yMn_zO_4$ materials. After 200 CVs scanning, decreased Tafel slope values (74−84 mV/dec) are shown, demonstrating the activation process resulted in better reaction kinetics on the oxide catalysts (Table S8). The values before and after activation are comparable to state-of-the-art Tafel slope values obtained for various transition metal oxides.[10]

A complementary method to probe the kinetics of the reactions is electrochemical impedance spectroscopy. Figures 6c and S12b represent the Nyquist plots of the activated oxides. A general model of the equivalent circuit for the metal oxides catalyzing OER was proposed by Lyons and co-workers.[62,63] This model, which was modified and applied in the work of Yu et al.,[39] is presented in Figure S13 and described in details in the Supporting Information (SI). The resistance response of the system consists of several parameters, including the solution resistance R_Ω, which has a value of ∼5 Ω for all oxides (Table S9). The polarization resistance (R_p) grows as the calcination temperature increases. $Ni_xCo_yMn_zO_4$-300 has the lowest value of R_p, which is related to the overall kinetics of OER. This is in line with the LSV results, which show that this sample is the most active. Moreover, $Ni_xCo_yMn_zO_4$-300 has the lowest value of R_s, while $Ni_xCo_yMn_zO_4$-500 has the highest one, being close to the value of $Ni_xCo_yMn_zO_4$-700 (Table S9). These results correlate with the change in the activity of the $Ni_xCo_yMn_zO_4$-500; i.e., after the activation process this sample almost did not show a decrease of the Tafel slope as compared to $Ni_xCo_yMn_zO_4$-300 (Figure 6a). Enhanced R_s values indicate issues occurring during the formation of the intermediate species for the OER. This could be related to the decrease of ordered mesoporosity and alteration of crystal and surface structures of the material obtained at a higher calcination temperature. The changed porosity of the initial materials might slow down diffusion processes making the rate of the intermediate species production slower. Another reason for the high R_s values for $Ni_xCo_yMn_zO_4$-500 might be that it is not favored to form active intermediate species for the OER from the mixture of the spinel phases formed at the temperature of 500 °C. However, this assumption requires further in-depth studies.

An important way to evaluate the intrinsic activity of the catalysts is to normalize the obtained current density by the ECSA and/or by BET SSA of the samples, as displayed in Figure S14a,b, respectively. Electrochemical double-layer capacitance (EDLC) and the corresponding ECSA values were extracted from cyclic voltammograms that were collected in the non-Faradaic region at different scan rates (20−180 mV/s) for every catalyst (Figure S15 and Table S10). A capacitive current difference at 1.05 V (vs RHE) is linearly related to the scan rate (Figures 6d and S16). An increase in the calcination temperature causes a general decrease trend in the ECSA value even if samples $Ni_xCo_yMn_zO_4$-300 and $Ni_xCo_yMn_zO_4$-500 have almost a similar one. However, once the current density was normalized by ECSA (Figure S14a), the activity trend changed. Indeed, $Ni_xCo_yMn_zO_4$-700 became the most active catalyst while $Ni_xCo_yMn_zO_4$-500 became the least active one. These results indicate that among the mixed oxides $Ni_xCo_yMn_zO_4$-700 provides the most active sites for OER catalysis. Differently, if the catalytic activity is normalized by SSA (Figure S14b), the trend remains similar to the initial one; i.e., $Ni_xCo_yMn_zO_4$-300 is the most active among all $Ni_xCo_yMn_zO_4$. These results indicate that there seem to be a higher number of active sites formed during the reaction using $Ni_xCo_yMn_zO_4$-300 as a catalyst, as compared to other samples. Moreover, the higher activity of $Ni_xCo_yMn_zO_4$-300 in LSV and SSA-normalized LSV might originate from better charge transfer, which is confirmed by EIS. In addition, $Ni_xCo_yMn_zO_4$-300 also exhibits the highest SSA (Table 1). The trend observed here is also in line with the assumption we made on the activity of the species of $Ni_xCo_yMn_zO_4$-500.

Stability of the catalyst was tested for the most active sample, $Ni_xCo_yMn_zO_4$-300, which was loaded on a Ni foam as a thin film. The Ni foam is a porous and highly conductive support, and loading a catalyst on its surface significantly improves the electrocatalytic performance due to enhanced mass and electron transfer.[64] As shown in Figure 6e, the activity of the $Ni_xCo_yMn_zO_4$-300 catalyst on Ni foam is higher than a pure Ni foam before and after 200 CVs, with the highest activity obtained after activation, being in line with results obtained with pure catalysts. The stability test was carried out over time at an applied current density of 10 mA/cm^2. The potential starts at 1.57 V and remains stable with a slight increase for over 15 h, demonstrating an appreciable stability of the catalyst (Figure 6f). Moreover, TEM images recorded after the stability test (Figure S17) confirm, despite the blurring effect of the KOH layer, the preservation of the 3D mesoporous structure with no major alteration and/or sintering. In the same way, spot EDX analysis (Table S11) showed the presence of Fe impurities on the surface of $Ni_xCo_yMn_zO_4$-300 after cycling, thus strengthening the idea of the activation process mentioned above,[60,61] whereby Fe impurities in KOH solution affect the activity of the Ni-containing materials.

■ DISCUSSION

To rationalize the electrocatalytic activity and stability of the $Ni_xCo_yMn_zO_4$ nanocasts, it is necessary to understand and correlate the effects of the synthesis parameters onto the physicochemical features of the materials. In this study, the influence of the calcination temperature of the metal precursors after being confined within the KIT-6 silica mesopores was investigated. Three different temperatures were used, i.e., 300, 500, and 700 °C. In every case, a relatively high specific surface area was obtained, confirming the efficiency of the nanocasting procedure to produce nanoporous electrocatalysts. Since all of the materials had fairly large mesopores, around 8−9 nm, the variation of the mode pore size induced by the calcination temperature did not seem to influence much the electrocatalytic behavior. As discussed above, no cavitation artifact was found in physisorption, indicating the absence of mass transfer/diffusion limitations connected with the presence of severe pore corrugations and/or ink-bottle-like pores. This result is in good correlation with recent works made on accessibility and diffusion within 3D pore networks.[15,44,65,66] Overall, a higher calcination temperature yielded mesoporous MTMOs with lower surface areas and total pore volumes but with larger NLDFT mode pore size. It could be correlated with the growth of larger crystal domains and a more pronounced shrinkage of the silica template structure. In contrast to the materials calcined at 300 and 500 °C, this effect is particularly noticeable at 700 °C due to further collapse of the mesoporous order, in addition to the growth of the metal oxide phase, of the KIT-6 silica structure (initially calcined at 550 °C only). It is thus important to take into account the potential alteration of the host material, especially if high-temperature treatments are applied, as confirmed by the low-angle XRD results. Higher temperatures will result in materials with poorer mesoscopic ordering. While the extent of the pore structuring importance is not yet fully understood for electrocatalysts, it appears that a more defined 3D pore network leads to more efficient and stable materials. This latter result is also related with the SSA as well as the overall mechanical and chemical stability of the pore structure. Using KIT-6 as a template, we were able to produce a mesoporous quaternary MTMOs, i.e., $Ni_xCo_yMn_zO_4$-300, with a BET SSA of about 200 m^2/g that exhibits interesting results and good stability over time. Most important, it also retained its mesostructure after electrocatalytic cycling for 15 h, demonstrating that it is possible to combine high porosity and appreciable durability.

Another important aspect is the crystallinity of the samples. Our results indicate that a lower degree of crystallinity, obtained using a moderate calcination temperature, is beneficial for the electrocatalyst, in good agreement with recent literature.[67] It was observed that moderate calcination temperatures lead to the formation of a mixture of the several oxides with spinel phases. Along the same way, lower calcination temperatures allow one to obtain samples with a higher surface concentration of Co^{3+} species. Such ions are important since their oxidation products, i.e., Co^{4+}, are known to facilitate the OER reaction.[58,67,68] Finally, as shown in Figure 6b, higher calcination temperatures lead to mesoporous MTMOs with higher Tafel slopes, indicating less favorable kinetics probably linked to the diminution of both the SSA and ECSA. It is thus not surprising for $Ni_xCo_yMn_zO_4$-700 to exhibit the lowest activity. Even if the electrocatalytic activity of this sample is the best of the series when normalized per ECSA, it was unlikely to synthesize a material with the pure $(Ni,Mn,Co)_3O_4$ spinel phase together with a high, or at least a comparable, ECSA to the other samples using such a high calcination temperature. On the contrary, moderate calcination temperatures (300 and 500 °C) yielded materials with statistically similar ECSA, with $Ni_xCo_yMn_zO_4$-300 further demonstrating the lowest electrochemical resistance, better kinetics of the reaction and best activity overall. While, overall, the performances of the quaternary oxides are not among the highest reported so far, with respect to Co_3O_4 and NiO samples, they still exhibit an OER activity per unit cost that is appealing. Highly active electrocatalysts for OER based on cobalt become unreliable and economically hazardous because of the rising issues with their supplies. Therefore, substitution of cobalt by other earth-abundant, cheap, and less toxic transition metals, such as Ni and Mn, appears as an attractive strategy for the development of novel, economically rationalized, and resource-friendly catalysts for OER. Another interesting aspect of the proposed electrocatalysts is their synthesis: $Ni_xCo_yMn_zO_4$-300 requires lower calcination temperatures in comparison to more active Co_3O_4 and NiO and may lead to substantial energy savings in the production stage. Thus, since its activity is still high enough for the intended purpose, this material can be seen as a promising model system to further explore different mixed metal catalysts toward OER. Indeed, synthesis strategies based on mixed transition metals will lead to important synergy effects that may enhance or even provide new properties to the resulting catalysts.[69] This part of the research toward the optimization of OER catalysts using cheap and abundant source materials is now actively explored and attracts large attention. In this way, extension of the synthesis recipes and further testing of the MTMOs calcined at lower temperatures as catalysts for oxygen reduction reaction and metal−air batteries are ongoing to evaluate and define their full potential.

CONCLUSION

Electrocatalytic performances of various quaternary mesoporous mixed metal oxide catalysts obtained via nanocasting were investigated. The best sample, $Ni_xCo_yMn_zO_4$ calcined at 300 °C, provided relatively high current density and low onset potential and overpotential, especially after activation, and delivered high current density once loaded into a Ni foam. This material also remained remarkably stable over 15 h of applied bias. In addition, correlations between the calcination temperature, pore and surface properties, phase and elemental composition, and the overall efficiency and stability of the electrocatalysts were established. The benefits of using a low calcination temperature were demonstrated, highlighting the potential of mixed metal oxides as catalysts for OER. Our results provide deeper insights and novel perspectives for the successful preparation of next generation cheap and efficient electrocatalysts.

ASSOCIATED CONTENT

Supporting Information

The Supporting Information is available free of charge at https://pubs.acs.org/doi/10.1021/acsaem.0c00544.

> XRD and powder patterns; physisorption isotherms; pore size distributions; TEM images; SEM and STEM images; Rietveld refinement; EDX analysis spots and values; CV data; LSV curves; Tafel slopes; Nyquist plot; equivalent circuit model; current density; C_{dl} plot and calculated values; capacitive current difference; Rietveld refinement results table; EDX and spot EDX data; current density, overpotential, and Tafel slope values; resistances fitted values; calculated electrochemical active surface area values (PDF)

AUTHOR INFORMATION

Corresponding Authors

Freddy Kleitz − *Department of Inorganic Chemistry—Functional Materials, Faculty of Chemistry, University of Vienna, A-1090 Wien, Austria;* orcid.org/0000-0001-6769-4180; Email: freddy.kleitz@univie.ac.at

Harun Tüysüz − *Department of Heterogeneous Catalysis, Max-Planck-Institut für Kohlenforschung, D-45470 Mülheim an der Ruhr, Germany;* orcid.org/0000-0001-8552-7028; Email: tueysuez@kofo.mpg.de

Authors

Tatiana Priamushko − *Department of Inorganic Chemistry—Functional Materials, Faculty of Chemistry, University of Vienna, A-1090 Wien, Austria*

Rémy Guillet-Nicolas − *Department of Inorganic Chemistry—Functional Materials, Faculty of Chemistry, University of Vienna, A-1090 Wien, Austria;* orcid.org/0000-0001-5971-4292

Mingquan Yu − *Department of Heterogeneous Catalysis, Max-Planck-Institut für Kohlenforschung, D-45470 Mülheim an der Ruhr, Germany;* orcid.org/0000-0001-5825-5370

Matthew Doyle − *Department of Inorganic Chemistry—Functional Materials, Faculty of Chemistry, University of Vienna, A-1090 Wien, Austria*

Claudia Weidenthaler − *Department of Heterogeneous Catalysis, Max-Planck-Institut für Kohlenforschung, D-45470 Mülheim an der Ruhr, Germany*

Complete contact information is available at:
https://pubs.acs.org/10.1021/acsaem.0c00544

Funding

T.P., R.G.-M., M.D., and F.K. acknowledge the funding support of the University of Vienna, Austria. This work was also financially supported partly by IMPRS-RECHARGE of Max Planck Society and by the Deutsche Forschungsgemeinschaft (DFG, German Research Foundation) Project No. 388390466-TRR 247 within the Collaborative Research Centre/Transregio 247 ("Heterogeneous Oxidation Catalysis in the Liquid Phase"). C.W. gratefully acknowledges basic funding of the MPG.

Notes

The authors declare no competing financial interest.

ACKNOWLEDGMENTS

S. Palm, H. Bongard, and A. Schlüter (MPI Mülheim) are acknowledged for EDX and electron microscopy analyses. T.P. also thoughtfully thanks Prof. Christian Lengauer from the Department of Mineralogy and Crystallography of the University of Vienna, Austria, for his help with the high-temperature PXRD measurements. Sebastian Leiting (MPI Mülheim) is acknowledged for XPS measurements.

ABBREVIATIONS

3D, three-dimensional
BET, Brunauer−Emmett−Teller method
CE, counter electrode
CV, cyclic voltammetry
ECSA, electrochemical active surface area
EDX, energy dispersive X-ray spectroscopy
GC, glassy carbon
HER, hydrogen evolution reaction
HR, high resolution
LSV, linear sweep voltammetry
MTMO, mixed transition metal oxide
NLDFT, non-local density functional theory
OER, oxygen evolution reaction
ORR, oxygen reduction reaction
PSD, pore size distribution
PXRD, powder X-ray diffraction
RDE, rotating disk electrode
RE, reference electrode
RHE, reversible hydrogen electrode
RRDE, rotating ring disk electrode
SEM, scanning electron microscopy
SSA, specific surface area
STEM, scanning transmission electrong microscopy
TEM, transmission electron microscopy
WE, working electrode
XPS, X-ray photoelectron spectroscopy

REFERENCES

(1) Antolini, E. Iridium as Catalyst and Cocatalyst for Oxygen Evolution/Reduction in Acidic Polymer Electrolyte Membrane Electrolyzers and Fuel Cells. *ACS Catal.* **2014**, *4*, 1426−1440.

(2) Surya, K.; Michael, M. S.; Prabaharan, S. R. S. A Review on Advancement in Non-Noble Metal Based Oxides as Bifunctional Catalysts for Rechargeable Non-Aqueous Li/Air Battery. *Solid State Ionics* **2018**, *317*, 89−96.

(3) Eftekhari, A.; Babu, V. J.; Ramakrishna, S. Photoelectrode Nanomaterials for Photoelectrochemical Water Splitting. *Int. J. Hydrogen Energy* **2017**, *42*, 11078−11109.

(4) Eftekhari, A. Tuning the Electrocatalysts for Oxygen Evolution Reaction. *Mater. Today Energy* **2017**, *5*, 37−57.

(5) Tahir, M.; Pan, L.; Idrees, F.; Zhang, X.; Wang, L.; Zou, J. J.; Wang, Z. L. Electrocatalytic Oxygen Evolution Reaction for Energy Conversion and Storage: A Comprehensive Review. *Nano Energy* **2017**, *37*, 136−157.

(6) Yan, Y.; Xia, B. Y.; Zhao, B.; Wang, X. A Review on Noble-Metal-Free Bifunctional Heterogeneous Catalysts for Overall Electrochemical Water Splitting. *J. Mater. Chem. A* **2016**, *4*, 17587−17603.

(7) Osgood, H.; Devaguptapu, S. V.; Xu, H.; Cho, J.; Wu, G. Transition Metal (Fe, Co, Ni, and Mn) Oxides for Oxygen Reduction and Evolution Bifunctional Catalysts in Alkaline Media. *Nano Today* **2016**, *11*, 601−625.

(8) Goswami, C.; Hazarika, K. K.; Bharali, P. Transition Metal Oxide Nanocatalysts for Oxygen Reduction Reaction. *Mater. Sci. Energy Technol.* **2018**, *1*, 117−128.

(9) Burke, M. S.; Zou, S.; Enman, L. J.; Kellon, J. E.; Gabor, C. A.; Pledger, E.; Boettcher, S. W. Revised Oxygen Evolution Reaction Activity Trends for First-Row Transition-Metal (Oxy)Hydroxides in Alkaline Media. *J. Phys. Chem. Lett.* **2015**, *6*, 3737−3742.

(10) Zhao, Q.; Yan, Z.; Chen, C.; Chen, J. Spinels: Controlled Preparation, Oxygen Reduction/Evolution Reaction Application, and Beyond. *Chem. Rev.* **2017**, *117*, 10121−10211.

(11) Løvik, A. N.; Hagelüken, C.; Wäger, P. Improving Supply Security of Critical Metals: Current Developments and Research in the EU. *Sustain. Mater. Technol.* **2018**, *15*, 9−18.

(12) Roche, I.; Chaînet, E.; Chatenet, M.; Vondrák, J. Durability of Carbon-Supported Manganese Oxide Nanoparticles for the Oxygen Reduction Reaction (ORR) in Alkaline Medium. *J. Appl. Electrochem.* **2008**, *38*, 1195−1201.

(13) Bikkarolla, S. K.; Yu, F.; Zhou, W.; Joseph, P.; Cumpson, P.; Papakonstantinou, P. A Three-Dimensional Mn_3O_4 Network Supported on a Nitrogenated Graphene Electrocatalyst for Efficient Oxygen Reduction Reaction in Alkaline Media. *J. Mater. Chem. A* **2014**, *2*, 14493−14501.

(14) Deng, X.; Rin, R.; Tseng, J.; Weidenthaler, C.; Apfel, U.; Tüysüz, H. Monodispersed Mesoporous Silica Spheres Supported Co_3O_4 as Robust Catalyst for Oxygen Evolution Reaction. *ChemCatChem* **2017**, *9*, 4238−4243.

(15) Fu, S.; Zhu, C.; Song, J.; Engelhard, M. H.; Li, X.; Du, D.; Lin, Y. Highly Ordered Mesoporous Bimetallic Phosphides as Efficient Oxygen Evolution Electrocatalysts. *ACS Energy Lett.* **2016**, *1*, 792−796.

(16) Deng, X.; Öztürk, S.; Weidenthaler, C.; Tüysüz, H. Iron-Induced Activation of Ordered Mesoporous Nickel Cobalt Oxide Electrocatalyst for the Oxygen Evolution Reaction. *ACS Appl. Mater. Interfaces* **2017**, *9*, 21225−21233.

(17) Broicher, C.; Zeng, F.; Artz, J.; Hartmann, H.; Besmehn, A.; Palkovits, S.; Palkovits, R. Facile Synthesis of Mesoporous Nickel Cobalt Oxide for OER − Insight into Intrinsic Electrocatalytic Activity. *ChemCatChem* **2019**, *11*, 412−416.

(18) Li, Y.; Zou, L.; Li, J.; Guo, K.; Dong, X.; Li, X.; Xue, X.; Zhang, H.; Yang, H. Synthesis of Ordered Mesoporous $NiCo_2O_4$ via Hard Template and Its Application as Bifunctional Electrocatalyst for Li-O_2 Batteries. *Electrochim. Acta* **2014**, *129*, 14−20.

(19) Ge, X.; Liu, Y.; Goh, F. W. T.; Hor, T. S. A.; Zong, Y.; Xiao, P.; Zhang, Z.; Lim, S. H.; Li, B.; Wang, X.; Liu, Z. Dual-Phase Spinel $MnCo_2O_4$ and Spinel $MnCo_2O_4$/Nanocarbon Hybrids for Electro-

catalytic Oxygen Reduction and Evolution. *ACS Appl. Mater. Interfaces* **2014**, *6*, 12684−12691.

(20) Yu, X.; Manthiram, A. $MnNiCoO_4$/N-MWCNT Nanocomposite Catalyst with High Selectivity in Membraneless Direct Formate Fuel Cells and Bifunctional Activity for Oxygen Electrochemistry. *Catal. Sci. Technol.* **2015**, *5*, 2072−2075.

(21) Sivakumar, P.; Subramanian, P.; Maiyalagan, T.; Gedanken, A.; Schechter, A. Ternary Nickel−cobalt−manganese Spinel Oxide Nanoparticles as Heterogeneous Electrocatalysts for Oxygen Evolution and Oxygen Reduction Reaction. *Mater. Chem. Phys.* **2019**, *229*, 190−196.

(22) Pendashteh, A.; Palma, J.; Anderson, M.; Marcilla, R. $NiCoMnO_4$ nanoparticles on N-Doped Graphene: Highly Efficient Bifunctional Electrocatalyst for Oxygen Reduction/Evolution Reactions. *Appl. Catal., B* **2017**, *201*, 241−252.

(23) Ren, Y.; Ma, Z.; Bruce, P. G. Ordered Mesoporous $NiMn_2O_x$ with Hematite or Spinel Structure: Synthesis and Application in Electrochemical Energy Storage and Catalytic Conversion of N_2O. *CrystEngComm* **2011**, *13*, 6955−6959.

(24) Rosen, J.; Hutchings, G. S.; Jiao, F. Ordered Mesoporous Cobalt Oxide as Highly Efficient Oxygen Evolution Catalyst. *J. Am. Chem. Soc.* **2013**, *135*, 4516−4521.

(25) Rumplecker, A.; Kleitz, F.; Salabas, E. L.; Schüth, F. Hard Templating Pathways for the Synthesis of Nanostructured Porous Co_3O_4. *Chem. Mater.* **2007**, *19*, 485−496.

(26) Deng, X.; Schmidt, W. N.; Tüysüz, H. Impacts of Geometry, Symmetry, and Morphology of Nanocast Co_3O_4 on Its Catalytic Activity for Water Oxidation. *Chem. Mater.* **2014**, *26*, 6127−6134.

(27) Yen, H.; Seo, Y.; Guillet-Nicolas, R.; Kaliaguine, S.; Kleitz, F. One-Step-Impregnation Hard Templating Synthesis of High-Surface-Area Nanostructured Mixed Metal Oxides ($NiFe_2O_4$, $CuFe_2O_4$ and Cu/CeO_2). *Chem. Commun.* **2011**, *47*, 10473−10475.

(28) Nair, M. M.; Yen, H.; Kleitz, F. Nanocast Mesoporous Mixed Metal Oxides for Catalytic Applications. *C. R. Chim.* **2014**, *17*, 641−655.

(29) Gu, D.; Schüth, F. Synthesis of Non-Siliceous Mesoporous Oxides. *Chem. Soc. Rev.* **2014**, *43*, 313−344.

(30) Ren, Y.; Ma, Z.; Bruce, P. G. Ordered Mesoporous Metal Oxides: Synthesis and Applications. *Chem. Soc. Rev.* **2012**, *41*, 4909.

(31) Deng, X.; Chen, K.; Tüysüz, H. Protocol for the Nanocasting Method: Preparation of Ordered Mesoporous Metal Oxides. *Chem. Mater.* **2017**, *29*, 40−52.

(32) Ren, Y.; Ma, Z.; Bruce, P. G. Ordered Mesoporous $NiCoMnO_4$: Synthesis and Application in Energy Storage and Catalytic Decomposition of N_2O. *J. Mater. Chem.* **2012**, *22*, 15121−15127.

(33) Ren, Y.; Ma, Z.; Qian, L.; Dai, S.; He, H.; Bruce, P. G. Ordered Crystalline Mesoporous Oxides as Catalysts for CO Oxidation. *Catal. Lett.* **2009**, *131*, 146−154.

(34) Yen, H.; Seo, Y.; Kaliaguine, S.; Kleitz, F. Tailored Mesostructured Copper/Ceria Catalysts with Enhanced Performance for Preferential Oxidation of CO at Low Temperature. *Angew. Chem., Int. Ed.* **2012**, *51*, 12032−12035.

(35) Yen, H.; Kleitz, F. High-Performance Solid Catalysts for H_2 Generation from Ammonia Borane: Progress through Synergetic Cu-Ni Interactions. *J. Mater. Chem. A* **2013**, *1*, 14790−14796.

(36) Lefrançois Perreault, L.; Colò, F.; Meligrana, G.; Kim, K.; Fiorilli, S.; Bella, F.; Nair, J. R.; Vitale-Brovarone, C.; Florek, J.; Kleitz, F.; Gerbaldi, C. Spray-Dried Mesoporous Mixed Cu-Ni Oxide@Graphene Nanocomposite Microspheres for High Power and Durable Li-Ion Battery Anodes. *Adv. Energy Mater.* **2018**, *8*, 1802438.

(37) Kleitz, F.; Choi, S. H.; Ryoo, R. Cubic Ia3d Large Mesoporous Silica: Synthesis and Replication to Platinum Nanowires, Carbon Nanorods and Carbon Nanotubes. *Chem. Commun.* **2003**, *17*, 2136−2137.

(38) Thommes, M.; Kaneko, K.; Neimark, A. V.; Olivier, J. P.; Rodriguez-Reinoso, F.; Rouquerol, J.; Sing, K. S. W. Physisorption of Gases, with Special Reference to the Evaluation of Surface Area and Pore Size Distribution (IUPAC Technical Report). *Pure Appl. Chem.* **2015**, *87*, 1051−1069.

(39) Yu, M.; Moon, G.; Bill, E.; Tüysüz, H. Optimizing Ni-Fe Oxide Electrocatalysts for Oxygen Evolution Reaction by Using Hard Templating as a Toolbox. *ACS Appl. Energy Mater.* **2019**, *2*, 1199−1209.

(40) Priamushko, T.; Guillet-Nicolas, R.; Kleitz, F. Mesoporous Nanocast Electrocatalysts for Oxygen Reduction and Oxygen Evolution Reactions. *Inorganics* **2019**, *7*, 98−119.

(41) Kondrashova, D.; Lauerer, A.; Mehlhorn, D.; Jobic, H.; Feldhoff, A.; Thommes, M.; Chakraborty, D.; Gommes, C.; Zecevic, J.; de Jongh, P.; Bunde, A.; Karger, J.; Valiullin, R. Scale-Dependent Diffusion Anisotropy in Nanoporous Silicon. *Sci. Rep.* **2017**, *7*, 40207.

(42) Grewe, T.; Deng, X.; Weidenthaler, C.; Schüth, F.; Tüysüz, H. Design of Ordered Mesoporous Composite Materials and Their Electrocatalytic Activities for Water Oxidation. *Chem. Mater.* **2013**, *25*, 4926−4935.

(43) Tüysüz, H.; Hwang, Y. J.; Khan, S. B.; Asiri, A. M.; Yang, P. Mesoporous Co_3O_4 as an Electrocatalyst for Water Oxidation. *Nano Res.* **2013**, *6*, 47−54.

(44) Sa, Y. J.; Kwon, K.; Cheon, J. Y.; Kleitz, F.; Joo, S. H. Ordered Mesoporous Co_3O_4 Spinels as Stable, Bifunctional, Noble Metal-Free Oxygen Electrocatalysts. *J. Mater. Chem. A* **2013**, *1*, 9992−10001.

(45) Zhao, H.; Liu, L.; Hu, Z.; Sun, L.; Han, S.; Liu, Y.; Chen, D.; Liu, X. Neutron Diffraction Analysis and Electrochemical Performance of Spinel $Ni(Mn_{2\text{-}X}Co_x)O_4$ as Anode Materials for Lithium Ion Battery. *Mater. Res. Bull.* **2016**, *77*, 265−270.

(46) Jiang, X.; Chu, S.; Chen, Y.; Zhong, Y.; Liu, Y.; Shao, Z. $LiNi_{0.29}Co_{0.33}Mn_{0.38}O_2$ polyhedrons with Reduced Cation Mixing as a High-Performance Cathode Material for Li-Ion Batteries Synthesized via a Combined Co-Precipitation and Molten Salt Heating Technique. *J. Alloys Compd.* **2017**, *691*, 206−214.

(47) Nair, M. M.; Kleitz, F.; Kaliaguine, S. Kinetics of Methanol Oxidation over Mesoporous Perovskite Catalysts. *ChemCatChem* **2012**, *4*, 387−394.

(48) Tüysüz, H.; Lehmann, C. W.; Bongard, H.; Tesche, B.; Schmidt, R.; Schuth, F. Direct Imaging of Surface Topology and Pore System of Ordered Mesoporous Silica (MCM-41, SBA-15, and KIT-6) and Nanocast Metal Oxides by High Resolution Scanning Electron Microscopy. *J. Am. Chem. Soc.* **2008**, *130*, 11510−11517.

(49) Ji, J.; Zhang, L. L.; Ji, H.; Li, Y.; Zhao, X.; Bai, X.; Fan, X.; Zhang, F.; Ruoff, R. S. Nanoporous $Ni(OH)_2$ Thin Film on 3D Ultrathin-Graphite Foam for Asymmetric Supercapacitor. *ACS Nano* **2013**, *7*, 6237−6243.

(50) Wang, G. H.; Deng, X.; Gu, D.; Chen, K.; Tüysüz, H.; Spliethoff, B.; Bongard, H. J.; Weidenthaler, C.; Schmidt, W.; Schüth, F. Co_3O_4 Nanoparticles Supported on Mesoporous Carbon for Selective Transfer Hydrogenation of α,β-Unsaturated Aldehydes. *Angew. Chem., Int. Ed.* **2016**, *55*, 11101−11105.

(51) Dangwal Pandey, A.; Jia, C.; Schmidt, W.; Leoni, M.; Schwickardi, M.; Schüth, F.; Weidenthaler, C. Size-Controlled Synthesis and Microstructure Investigation of Co_3O_4 Nanoparticles for Low-Temperature CO Oxidation. *J. Phys. Chem. C* **2012**, *116*, 19405−19412.

(52) Jia, C. J.; Schwickardi, M.; Weidenthaler, C.; Schmidt, W.; Korhonen, S.; Weckhuysen, B. M.; Schüth, F. Co_3O_4-SiO_2 Nanocomposite: A Very Active Catalyst for CO Oxidation with Unusual Catalytic Behavior. *J. Am. Chem. Soc.* **2011**, *133*, 11279−11288.

(53) Alonso, E.; Gallo, A.; Pérez-Rábago, C.; Fuentealba, E. Thermodynamic Study of CuO/Cu_2O and Co_3O_4/CoO Redox Pairs for Solar Energy Thermochemical Storage. *AIP Conf. Proc.* **2015**, *1734*, 050004.

(54) Lu, J.; Huang, C.; Bai, S.; Jiang, Y.; Li, Z. Thermal Decomposition and Cobalt Species Transformation of Carbon Nanotubes Supported Cobalt Catalyst for Fischer−Tropsch Synthesis. *J. Nat. Gas Chem.* **2012**, *21*, 37−42.

(55) Biesinger, M. C.; Payne, B. P.; Grosvenor, A. P.; Lau, L. W. M.; Gerson, A. R.; Smart, R. S. C. Resolving Surface Chemical States in

XPS Analysis of First Row Transition Metals, Oxides and Hydroxides: Cr, Mn, Fe, Co and Ni. *Appl. Surf. Sci.* **2011**, *257*, 2717−2730.

(56) McCrory, C. C. L.; Jung, S.; Ferrer, I. M.; Chatman, S. M.; Peters, J. C.; Jaramillo, T. F. Benchmarking Hydrogen Evolving Reaction and Oxygen Evolving Reaction Electrocatalysts for Solar Water Splitting Devices. *J. Am. Chem. Soc.* **2015**, *137*, 4347−4357.

(57) Yeo, B. S.; Bell, A. T. Enhanced Activity of Gold-Supported Cobalt Oxide for the Electrochemical Evolution of Oxygen. *J. Am. Chem. Soc.* **2011**, *133* (14), 5587−5593.

(58) Qu, Q.; Zhang, J. H.; Wang, J.; Li, Q. Y.; Xu, C. W.; Lu, X. Three-Dimensional Ordered Mesoporous Co_3O_4 Enhanced by Pd for Oxygen Evolution Reaction. *Sci. Rep.* **2017**, *7*, 41542.

(59) McAlpin, J. G.; Surendranath, Y.; Dincã, M.; Stich, T. A.; Stoian, S. A.; Casey, W. H.; Nocera, D. G.; Britt, R. D. EPR Evidence for Co(IV) Species Produced during Water Oxidation at Neutral PH. *J. Am. Chem. Soc.* **2010**, *132*, 6882−6883.

(60) Dionigi, F.; Strasser, P. NiFe-Based (Oxy)Hydroxide Catalysts for Oxygen Evolution Reaction in Non-Acidic Electrolytes. *Adv. Energy Mater.* **2016**, *6*, 1600621.

(61) Li, N.; Bediako, D. K.; Hadt, R. G.; Hayes, D.; Kempa, T. J.; Von Cube, F.; Bell, D. C.; Chen, L. X.; Nocera, D. G. Influence of Iron Doping on Tetravalent Nickel Content in Catalytic Oxygen Evolving Films. *Proc. Natl. Acad. Sci. U. S. A.* **2017**, *114*, 1486−1491.

(62) Doyle, R. L.; Godwin, I. J.; Brandon, M. P.; Lyons, M. E. G. Redox and Electrochemical Water Splitting Catalytic Properties of Hydrated Metal Oxide Modified Electrodes. *Phys. Chem. Chem. Phys.* **2013**, *15*, 13737−13783.

(63) Doyle, R. L.; Lyons, M. E. G. An Electrochemical Impedance Study of the Oxygen Evolution Reaction at Hydrous Iron Oxide in Base. *Phys. Chem. Chem. Phys.* **2013**, *15*, 5224−5237.

(64) Tang, C.; Cheng, N.; Pu, Z.; Xing, W.; Sun, X. NiSe Nanowire Film Supported on Nickel Foam: An Efficient and Stable 3D Bifunctional Electrode for Full Water Splitting. *Angew. Chem., Int. Ed.* **2015**, *54*, 9351−9355.

(65) Hu, C.; Dai, L. Multifunctional Carbon-Based Metal-Free Electrocatalysts for Simultaneous Oxygen Reduction, Oxygen Evolution, and Hydrogen Evolution. *Adv. Mater.* **2017**, *29*, 1604942.

(66) Li, Y.; Zhao, M.; Zhao, Y.; Song, L.; Zhang, Z. FeNi Layered Double-Hydroxide Nanosheets on a 3D Carbon Network as an Efficient Electrocatalyst for the Oxygen Evolution Reaction. *Part. Part. Syst. Charact.* **2016**, *33*, 158−166.

(67) Moon, G.; Yu, M.; Chan, C. K.; Tüysüz, H. Highly Active Cobalt-Based Electrocatalysts with Facile Incorporation of Dopants for the Oxygen Evolution Reaction. *Angew. Chem.* **2019**, *131*, 3529−3533.

(68) Lu, X.; Ng, Y. H.; Zhao, C. Gold Nanoparticles Embedded within Mesoporous Cobalt Oxide Enhance Electrochemical Oxygen Evolution. *ChemSusChem* **2014**, *7*, 82−86.

(69) Shi, J. On the Synergetic Catalytic Effect in Heterogeneous Nanocomposite Catalysts. *Chem. Rev.* **2013**, *113*, 2139−2181.